

Two-photon polymerization of femtosecond high-order Bessel beams with aberration correction

Erse Jia (贾而稿)¹, Chen Xie (谢辰)^{1*}, Na Xiao (肖娜)¹, Francois Courvoisier², and Minglie Hu (胡明列)¹

¹Ultrafast Laser Laboratory, Key Laboratory of Opto-electronic Information Technical Science of Ministry of Education, School of Precision Instruments and Opto-electronics Engineering, Tianjin University, Tianjin 300072, China

²FEMTO-ST Institute, Université de Bourgogne-Franche-Comté UMR-6174, 25030 Besançon, France

*Corresponding author: xie_chen@tju.edu.cn

Received February 16, 2023 | Accepted April 18, 2023 | Posted Online July 20, 2023

In the femtosecond two-photon polymerization (2PP) experimental system, optical aberrations degrade the fabrication quality. To solve this issue, a multichannel interferometric wavefront sensing technique is adopted in the adaptive laser processing system with a single phase-only spatial light modulator. 2PP fabrications using corrected high-order Bessel beams with the above solution have been conducted, and high-quality microstructure arrays of microtubes with 20 μm diameter have been rapidly manufactured. The effectiveness of the proposed scheme is demonstrated by comparing the beam intensity distributions and 2PP results before and after aberration corrections.

Keywords: femtosecond laser; two-photon polymerization; aberration correction; Bessel beams.

DOI: [10.3788/COL202321.071203](https://doi.org/10.3788/COL202321.071203)

1. Introduction

Femtosecond two-photon polymerization (2PP)^[1-5] is widely used in the fabrication of three-dimensional complex architectures with a submicrometer resolution. Recent applications are templates for quantum dots^[6], scanning-probe microscopes^[7], microchips^[8], and biomimetic 4D printing^[9]. The conventional 2PP procedures utilize the tightly focused femtosecond laser beam to trigger polymerization inside the photoresist. In recent years, femtosecond 2PP based on adaptive optics^[10-13] has attracted considerable interest due to enhanced fabrication efficiency with different structured light beams, such as Bessel beams^[14], optical vortex beams^[15-17], abruptly autofocusing beams^[18], and axilens beams with long focal depths^[19]. Within these procedures, the spatial light modulators (SLMs) are introduced to generate arbitrary optical patterns through a computer-generated hologram (CGH) algorithm^[20] so that various structures could be fabricated via a one-step exposure. In fact, many factors in the 2PP setup combining an ultrafast laser and adaptive optics can introduce undesired aberrations, such as the walk-off effect in the nonlinear crystal, the internal stress and nonlinear response of the adaptive devices, and the manufacturing defects or assembly errors of the optical element.

On the other side, Bessel beams are notable for the diffraction resistance and self-healing behaviors. Besides these properties, high-order Bessel beams also show the potential to synthesize more complex structured light^[21,22]. Based on the above characteristics, high-order Bessel beams have been widely used in

micronanomanufacturing^[23], biological imaging^[24], optical tweezers^[25], optical communication^[26,27], and other fields. However, the aberrations in the setup significantly affect the application of high-order Bessel beams, since their patterns are extremely sensitive to aberrations^[28].

Numerous methods can assist in shaping beams and/or removing aberrations in the optical system^[29-34], and SLMs are the critical devices in these adaptive methods. Crucially, these solutions all require relatively advanced mathematical tools, such as the Zernike polynomial, the Gerchberg-Saxton, or more complex algorithms. In the application of waveguide writing, the SLM has shown great power in correcting the spherical aberration inside bulky glass^[34] and controlling nonlinear propagation^[34,35]. Despite the negligible nonlinear propagating effect in the application of 2PP, SLMs are also playing critical roles by building fabricating systems based on adaptive optics. In such systems, a relay optics system is installed after the SLM to generate micrometer-scaled structured beams. Further filterings are usually introduced to eliminate the undesired diffracting subbeams resulting from the superimposed grating phases. Therefore, considering the increased complexity of these systems caused by the pixelated SLM, the above aberration correction approaches will no longer be applicable.

In this paper, we demonstrate the power of aberration correction in our 2PP experimental system based on the multichannel interferometric wavefront sensing technique. This method was originally developed to restore the intensity distribution of the structured beams *in situ*^[36], requiring no complex mathematical

tools. A single phase-only SLM is sufficient to implement this method into optimizing the 2PP system, sparing the heavy work of alignments in installing the system. We verify the effectiveness of this method by comparing the intensity profiles of the high-order Bessel beam before and after the correction. The experimental results of our aberration-free structured beam present excellent agreement with the simulations in the ideal case. With the help of this method, we finally realize the rapid fabrication of high-quality microtube structures by directly exposing the high-order Bessel beams to the negative photoresist.

2. Principle of the Aberration Correction

Any given optical field propagating through an optical system can be expressed as a composition of modes in any orthogonal representation^[36]. The optimal focusing is achieved if and only if all the modes present the identical phase, which means the strength of constructive interference would be highest between these modes. Therefore, optimal focusing generally requires accurately compensating for the phase of each mode for any beam in the physical setup with imperfect optics. As an adaptive programmable device, the liquid crystal-based SLM can perform versatile tasks, including structured light generation and optical field detection and/or correction. In our setup, we divide the two-dimensional pixel array on the SLM into $M \times N$ channels with equal size. Each channel is filled with a blazed grating phase with an independent on-off switch, as shown in Figs. 1(a) and 1(b). With the blazed grating phase, the modulating information in each channel is coded in the first-order diffracting light and spatially separated from the undesired zeroth-order light. In the procedure of wave-front sensing, we first select a channel as the phase reference and keep this channel on. Then, all the other test

channels are successively switched on along the direction shown in Fig. 1(b). The intensity signal in the focal plane of the lens is collected while increasing the phase of the tested channel from 0 to 2π . For convenience, the amplitude and phase of the i th test channel and reference channel are, respectively, denoted by $|U_i|$, φ_i and $|U_r|$, φ_r . The interference intensity I of the first order of diffraction would follow the relation

$$I \propto |U_i|^2 + |U_r|^2 + 2|U_i||U_r| \cos(\varphi_i - \varphi_r). \quad (1)$$

Therefore, the phase of the test channel φ_i will be identical with the reference φ_r when the signal tends to reach the maximum. Note that the phase terms in Eq. (1) represent the phase profiles in each channel, which is assumed as nearly homogeneous across the corresponding subregional wavefront. After probing all the test channels, the full wavefront would be plotted, and a complementary phase map would be readily loaded on the SLM [Fig. 1(c)] to achieve aberration compensation. A specific example of correction is shown in Figs. 1(c)–1(e), with details explained in the following section.

3. Experiments and Results

3.1. Setup

The above aberration detection scheme could be readily integrated in our setup for 2PP, as shown in Fig. 2. The laser source is a home-made femtosecond fiber laser amplifying system with standard double-cladding fibers similar to that in Ref. [37], enabling 90-fs transform-limited laser pulses centered at 1038 nm output at 1-MHz repetition rate. A BBO crystal is inserted to generate the second-harmonic (SH) wave for the 2PP fabricating process. Considering the damage threshold of the coating on the crystal surface, the fabrication does not require the femtosecond laser to work at full load. After expansion, the SH wave of a diameter ~ 8 mm illuminates the phase-only SLM (Holoeye PLUTO, 1920 pixels \times 1080 pixels) with the exposed power

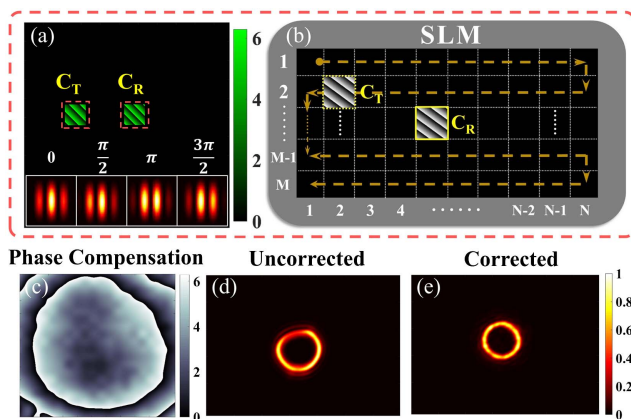


Fig. 1. Schematics of the wavefront sensing. (a) Two channels on the SLM; C_T , test channel; C_R , reference channel; insets in (a) show the simulated interference patterns with various phase differences between the test and the reference channels: 0 , $\pi/2$, π , and $3\pi/2$. (b) SLM area division and scanning path of the test channel; (c) aberration correction mask loaded on the SLM; Fourier spectral profiles of the high-order Bessel beams (d) before and (e) after the correction.

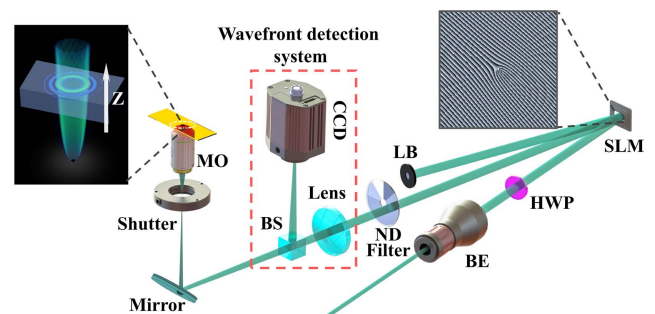


Fig. 2. Schematic of the setup. BE, beam expander; HWP, half-wave plate; SLM, spatial light modulator; LB, laser block; ND filter, neutral-density filter; BS, beam splitter; Shutter, mechanical shutter; MO, microscope objective; CCD, CCD camera. Inset close to the SLM presents the phase pattern to generate the Bessel vortex beams; the corresponding 3D light fields at the focus area in the slide are presented in the inset close to MO.

adjusted by the neutral density (ND) filter. The telescope composed by the lens ($f = 1$ m) and the microscope objective (Olympus 20 \times , NA = 0.4) shrinks the modulated waves into the microscaled patterns. A mechanical shutter is used to control the exposure time in the sample. The CCD camera is located at the focal plane of the lens to perform the wavefront detection.

In order to achieve more accurate wavefront detection, the number of divided areas on the SLM is, in principle, the larger the better. However, a single channel with very few pixels would be too problematic to implement, resulting in too weak intensity of the interference patterns to be detected. Since the optical aberration in a typical device is a smooth function with low spatial frequencies, dividing the pixel panel into no fewer than 10×10 channels can provide sufficient sampling. To ensure the fineness of the detected wavefront, we divided the SLM panel into 20×20 channels in our tests together with $\pi/10$ phase increment. After probing the whole panel with the scheme in the previous section, we obtain the compensating phase, as shown in Fig. 1(c). We note here that no great effort is made in aligning the beam path, leading to a significant aberration introduced in terms of misalignment. It is noteworthy that more than 4π phase fluctuations across the beam are detected, and thus a highly distorted field from the desired pattern would be expected. We remark that a high-quality objective from Olympus is adopted in the current setup to suppress the aberrations after the long focal lens in the telescope. But it is also possible to correct the aberration of the whole optical system with our scheme by inserting another lens after the objective and monitoring the signal in its focal plane. This is not realized in the current setup due to the rather limited space. Further engineering the setup is also part of our future work.

3.2. Aberration correction

As in Ref. [38], we apply the phase below on the input beam to generate high-order Bessel beams,

$$\varphi(r, \theta) = -k \sin(\gamma)r + m\theta, \quad (2)$$

where k is the wave vector in vacuum, γ is the cone angle between the refracted conical wave and the optical axis, and m is the vortex order. In this paper, we take $m = 6$ and $\gamma = 4^\circ$. Note that a blazed grating phase was also added to the SLM to separate the desired beam from the unmodulated zeroth-order light^[39]. The Fourier spectra of the Bessel beams are further recorded, showing the distorted profile without correction in Fig. 1(d). After superimposing the compensating mask, the Fourier spectra are well corrected in terms of both circularity and intensity uniformity [Fig. 1(e)]. In addition, a slightly shrunk radius also occurs after the correction, which can be explained by the overall converging property of the compensating phase map.

Figure 3 presents the longitudinal and transverse intensity profiles of our high-order Bessel beams in direct space after the microscope objective (MO) in Fig. 2. Numeric results of the Bessel beams generated from an ideal Gaussian beam are presented in the first row of Fig. 3 for comparison. The

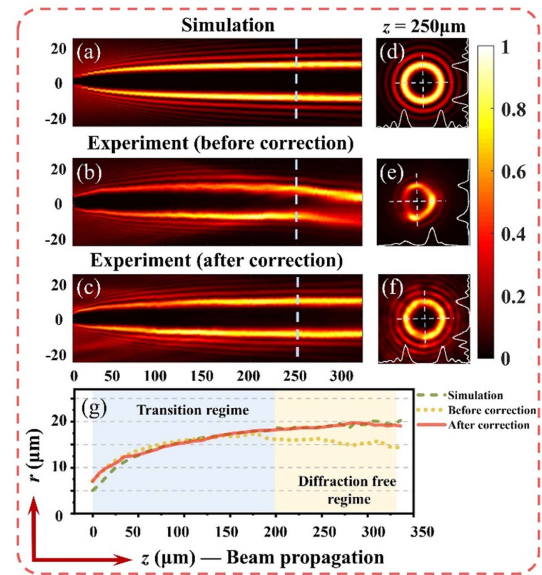


Fig. 3. Correction of the high-order Bessel beams with vortex charge $m = 6$; the longitudinal intensity profiles along propagation (a) in simulation and in experiments (b) before and (c) after the correction; corresponding transverse intensity profiles at $z = 250 \mu\text{m}$ in (d)–(f); (g) evolution of the main lobe size along the propagation.

simulations are performed based on the angular spectrum method, as in our previous studies^[38,40]. The second and third rows show the corresponding intensity profiles in experiments before and after the correction, respectively. After the transitionally expanding region along propagation^[38,40], the main lobe converges to a constant diameter ($\sim 20 \mu\text{m}$) in the nondiffracting regime, as shown in Fig. 3(g). However, the uncorrected main lobe cannot maintain its nondiffracting feature, as shown in Fig. 3(b). Meanwhile, the annular intensity profile has also been seriously distorted with fewer annular rings. As expected, the correction operation has significantly reduced the detrimental aberrations, as shown in Figs. 3(c) and 3(f). The shape of the central intensity tube returns to the ideal trajectory, and the intensity profile also restores its original pattern. Overall, the high-order Bessel beams after aberration correction are highly consistent with the ideal beam in the simulation.

3.3. Results and analyses

Encouraged by the high consistency between the restored and the ideal beam profile, we perform the 2PP as a further test. In the 2PP fabrication, the negative photoresist (MicroChem SU-8 2075, diluted with cyclopentanone, with the ratio of SU-8 : cyclopentanone = 5 : 1) is uniformly spin-coated on the glass slide substrate at 1500 r/min. Soft baking was performed on a hot plate for 5 min at 65°C and then for 10 min at 95°C . Up to 1.5 mW average power of the ultrafast SH wave is exposed in the prepared sample at 1-MHz repetition rate, corresponding to 1.5 nJ single-pulse energy. The relatively low repetition rate can avoid the occurrence of a thermal issue in the manufacturing process well. Considering that the transitionally expanding ring

lobe along propagation may occur more significantly for Bessel beams of certain parameters, as shown in Fig. 3 and discussed in our previous work^[38,40], the nondiffracting region should be carefully positioned to cross the whole photoresist layer to guarantee the fabrication of well-shaped microtubes, as shown in the inset of Fig. 2. Once the axial position of the beam is well selected, transversal movement in the horizontal plane together with exposure at proper power level would allow the rapid fabrication of the microtube array. The average time to fabricate each single microtube, including the movement and the exposure, is no more than 0.8 s without optimization. After the hard baking following the exposure, the photoresist is developed to produce micropatterns as high as 30 μm , as shown in Fig. 4.

The scanning electron microscopy (SEM) images of the microtubes are obtained with ZEISS Gemini 300 electronic microscope, as shown in Fig. 4. For comparison, we first perform the fabrication of microtubes with the uncorrected high-order Bessel beams of vortex charge $m = 6$. It can be seen in Figs. 4(a)–4(c) that the microtubes are seriously deformed due to the uncorrected Bessel beams in the nondiffraction region, as shown in Fig. 3. Figures 4(d)–4(f) present the microtube arrays with the single units fabricated by aberration-free high-order Bessel beams. It is apparent that the uniformity of the fabricated units is very satisfying. The measured outer ring diameters and wall thickness of the microstructures are $\sim 20.8 \mu\text{m}$ and $\sim 4.3 \mu\text{m}$, respectively.

The white dashed lines with arrows in Figs. 4(c) and 4(f) outline the outer walls of the microtubes before and after the aberration correction. It is noteworthy that the aberration also leads to the tapered wall in Fig. 4(c), i.e., a transitional polymerization region between the glass substrate and the microtube bottom. Most importantly, the nonuniform intensity of the uncorrected main lobe would introduce a much higher fluctuation of the local intensity during the 2PP process, which further degrades the inconsistency of the microtube wall thickness. In addition, we also found that the microtubes with nonuniform-shaped walls have higher rates to fall down on the glass substrate. We attribute this to the structural shrinkage induced by the nonuniform light energy deposition along the distorted Bessel beams, as shown in Fig. 3^[41]. After the phase correction, the above issues are well addressed. Once the high-order Bessel beams are well

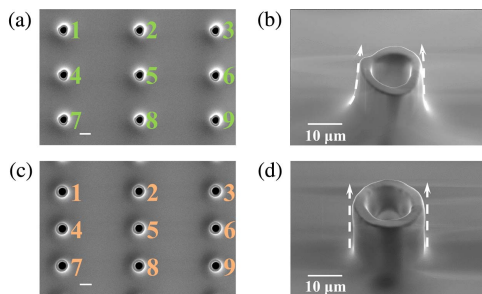


Fig. 4. SEM photos of microtube structures fabricated with high-order Bessel beams. (a), (b) Before and (c), (d) after aberration correction; the scaling bars without notation represent 20 μm .

positioned across the interface between the substrate and the photoresist, no falling-down of the microtube structures is observed.

In order to quantify the improvement in fabrication quality after the aberration removal, we extract the contours of the inner and outer rings of the microstructures in the SEM photos and measure their circularity. The ring contours are extracted by a combination of conventional operations in digital image processing, such as binarization, smoothing, filling, and edge detection. The definition of circularity adopted here is: $C = 4\pi \times A/P^2$, where A and P represent the area and perimeter of the selected contour, respectively. Obviously, the C value closer to unity indicates that the geometrical shape of the corresponding contour is closer to an ideal circle. Figure 5 presents the circularity characterizations of the microtubes with identification numbers in Figs. 4(a) and 4(d). The average circularities of the outer rings before and after the correction are 0.919 and 0.893, accompanying those of the corresponding inner rings, 0.956 and 0.939, respectively. It is worth noting that compared with the inner rings, the outer rings are more sensitive to the aberration in our setup.

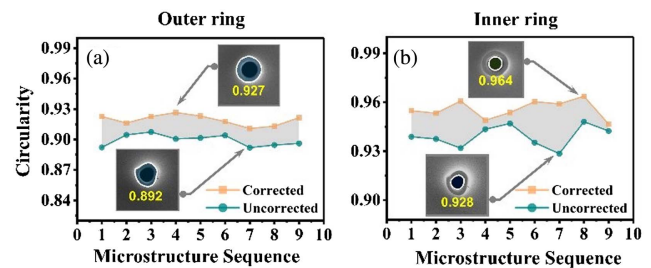


Fig. 5. Circularity measurement results of the microtube structures. (a) Outer rings and (b) inner rings.

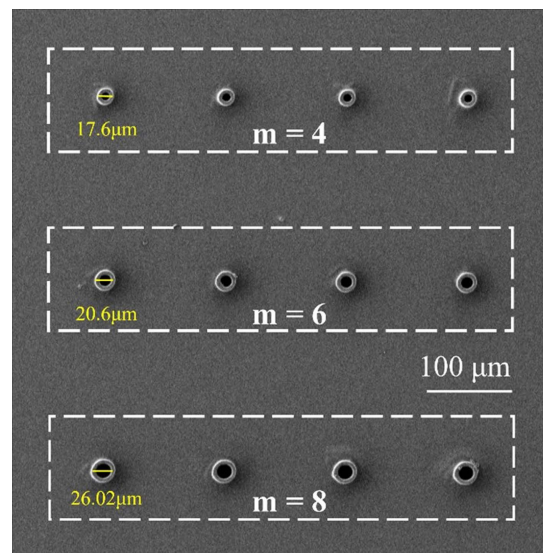


Fig. 6. SEM photos of microtubes fabricated with high-order Bessel beams of different vortex charges.

It is widely known that the vortex charge m can also affect the size of the main intensity lobe. To demonstrate the validity of this approach, we also fabricate microtubes with Bessel beams of different vortex charges. In the fabrication, the laser power and the exposure time are adapted accordingly, due to the change of the lobe size. Figure 6 presents the SEM images of microtubes fabricated by high-order Bessel beams with vortex charges of 4, 6, and 8, and the measured outer rings diameters are 17.6, 20.6, and 26.06 μm , respectively. All of the microtube structures present high-quality roundness and robust attachment to the substrate.

4. Conclusion

In this paper, we have demonstrated the powerful feasibility of the multichannel interference wavefront sensing in adaptive-optics-based 2PP. To demonstrate this, significant aberrations are intentionally introduced in the installation of our home-built system for ultrafast laser processing without great effort. Without an additional wavefront sensor, more than 4π wavefront fluctuation across the input beam can be well flattened with the integration of the above wavefront sensing scheme. This results in significant improvement of fabrication quality with corrected high-order Bessel beams. Since the integration of this wavefront-sensing technique requires no knowledge of advanced mathematical skills for workers, such as Zernike-polynomial-based decomposition, Gerchberg–Saxton iteration, and/or more complex algorithms, this straightforward solution would be highly attractive to implement in a laser processing system based on adaptive optics. In addition, our work also shows a promising perspective on significantly lowering the cost of the fabricating system by sparing the ultrafast lasers with super high-quality beams and exhausting alignments. We envision that our work will be very attractive in the broader scope of laser processing, where a well-defined wavefront is desired, such as femtosecond laser-induced periodic surface structures^[42]. For the present, the wavefront correction is performed just before the fabrication without any real-time feedback during the printing process. But we also notice that a novel monitoring method would allow real-time monitoring of the printing^[43]. We remark that this method together with our technique would be a good solution to correcting not only the aberration from the optical systems, but also the distortions from other factors in the fabricating process. Future works may also contribute to the fine feature correction with complex amplitude modulation.

Acknowledgement

This work was supported by the National Natural Science Foundation of China (Nos. 62275191, 61605142, and 61827821); the Tianjin Research Program of Application Foundation and Advanced Technology of China (No. 17JCJC43500); the Open Fund of the State Key Laboratory of High Field Laser Physics, Shanghai Institute of Optics and Fine Mechanics, Chinese Academy of Sciences;

the European Research Council (No. 682032-PULSAR); and the Agence Nationale de la Recherche (Nos. ANR-15-IDEX-0003 and ANR-17-EURE-0002).

References

1. S. Kawata, H. Sun, T. Tanaka, and K. Takada, "Finer features for functional microdevices," *Nature* **412**, 697 (2001).
2. L. Jiang, W. Xiong, Y. Zhou, Y. Liu, X. Huang, D. Li, T. Baldacchini, L. Jiang, and Y. Lu, "Performance comparison of acrylic and thiol-acrylic resins in two-photon polymerization," *Opt. Express* **24**, 13687 (2016).
3. W. Chu, Y. Tan, P. Wang, J. Xu, W. Li, J. Qi, and Y. Cheng, "Centimeter-height 3D printing with femtosecond laser two-photon polymerization," *Adv. Mater. Technol.* **3**, 1700396 (2018).
4. L. Li, R. Gattass, E. Gershgoren, H. Hwang, and J. Fourkas, "Achieving $\lambda/20$ resolution by one-color initiation and deactivation of polymerization," *Science* **324**, 910 (2009).
5. T. Frenzel, M. Kadic, and M. Wegener, "Three-dimensional mechanical metamaterials with a twist," *Science* **358**, 1072 (2017).
6. A. Bogucki, L. Zinkiewicz, M. Grzeszczyk, W. Pacuski, K. Nogajewski, T. Kazimierzczuk, A. Rodek, J. Suffczyński, K. Watanabe, T. Taniguchi, P. Wasylczyk, M. Potemski, and P. Kossacki, "Ultra-long-working-distance spectroscopy of single nanostructures with aspherical solid immersion microlenses," *Light Sci. Appl.* **9**, 48 (2020).
7. P. Dietrich, G. Göring, M. Trappen, M. Blaicher, W. Freude, T. Schimmel, H. Hölscher, and C. Koos, "3D-printed scanning-probe microscopes with integrated optical actuation and read-out," *Small* **16**, 1904695 (2019).
8. C. Wang, L. Yang, C. Zhang, S. Rao, Y. Wang, S. Wu, J. Li, Y. Hu, D. Wu, J. Chu, and K. Sugioka, "Multilayered skyscraper microchips fabricated by hybrid "all-in-one" femtosecond laser processing," *Microsyst. Nanoeng.* **5**, 17 (2019).
9. Z. Ma, Y. Zhang, B. Han, X. Hu, C. Li, Q. Chen, and H. Sun, "Femtosecond laser programmed artificial musculoskeletal systems," *Nat. Commun.* **11**, 4536 (2020).
10. P. S. Salter and M. J. Booth, "Adaptive optics in laser processing," *Light Sci. Appl.* **8**, 110 (2019).
11. S. Gittard, A. Nguyen, K. Obata, A. Koroleva, R. Narayan, and B. Chichkov, "Fabrication of microscale medical devices by two-photon polymerization with multiple foci via a spatial light modulator," *Biomed. Opt. Express* **2**, 3167 (2011).
12. X. Li, Y. Cao, N. Tian, L. Fu, and M. Gu, "Multifocal optical nanoscopy for big data recording at 30 TB capacity and gigabits/second data rate," *Optica* **2**, 567 (2015).
13. P. Salter and M. Booth, "Dynamic control of directional asymmetry observed in ultrafast laser direct writing," *Appl. Phys. Lett.* **101**, 141109 (2012).
14. L. Yang, A. El-Tamer, U. Hinze, J. Li, Y. Hu, W. Huang, J. Chu, and B. Chichkov, "Two-photon polymerization of cylinder microstructures by femtosecond Bessel beams," *Appl. Phys. Lett.* **105**, 041110 (2014).
15. B. Mills, D. Kundys, M. Farsari, S. Mailis, and R. W. Eason, "Single-pulse multiphoton fabrication of high aspect ratio structures with sub-micron features using vortex beams," *Appl. Phys. A* **108**, 651 (2012).
16. E. Stankevicius, T. Gertus, M. Rutkauskas, M. Gedvilas, G. Raciukaitis, R. Gadonas, V. Smilgevicius, and M. Malinauskas, "Fabrication of microtube arrays in photopolymer SZ2080 by using three different methods of a direct laser polymerization technique," *J. Micromech. Microeng.* **22**, 065022 (2012).
17. L. Yang, D. Qian, C. Xin, Z. Hu, S. Ji, D. Wu, Y. Hu, J. Li, W. Huang, and J. Chu, "Direct laser writing of complex microtubes using femtosecond vortex beams," *Appl. Phys. Lett.* **110**, 221103 (2017).
18. M. Manousidaki, D. Papazoglou, M. Farsari, and S. Tzortzakakis, "Abruptly autofocusing beams enable advanced multiscale photo-polymerization," *Optica* **3**, 525 (2016).
19. D. Pan, S. Liu, S. Ji, Z. Cai, J. Li, Y. Hou, W. Zhang, S. Fan, R. Li, Y. Hu, W. Zhu, D. Wu, and J. Chu, "Efficient fabrication of a high-aspect-ratio AFM tip by one-step exposure of a long focal depth holographic femtosecond axilens beam," *Opt. Lett.* **45**, 897 (2020).

20. D. Yang, L. Liu, Q. Gong, and Y. Li, "Rapid two-photon polymerization of an arbitrary 3D microstructure with 3D focal field engineering," *Macromol. Rapid Comm.* **40**, 1900041 (2019).
21. G. Kontenis, D. Gailevičius, N. Jiménez, and K. Staliunas, "Optical drills by dynamic high-order Bessel beam mixing," *Phys. Rev. Appl.* **17**, 034059 (2022).
22. V. Anand, S. Khonina, R. Kumar, N. Dubey, A. N. K. Reddy, J. Rosen, and S. Juodkazis, "Three-dimensional incoherent imaging using spiral rotating point spread functions created by double-helix beams [Invited]," *Nanoscale Res. Lett.* **17**, 37 (2022).
23. B. Wetzel, C. Xie, P. Lacourt, J. M. Dudley, and F. Courvoisier, "Femtosecond laser fabrication of micro and nano-disks in single layer graphene using vortex Bessel beams," *Appl. Phys. Lett.* **103**, 241111 (2013).
24. W. Yu, Z. Ji, D. Dong, X. Yang, Y. Xiao, Q. Gong, P. Xi, and K. Shi, "Super-resolution deep imaging with hollow Bessel beam STED microscopy," *Laser Photonics Rev.* **10**, 147 (2016).
25. K. Volke-Sepulveda, V. Garcés-Chávez, S. Chávez-Cerda, J. Arlt, and K. Dholakia, "Orbital angular momentum of a high-order Bessel light beam," *J. Opt. B* **4**, S82 (2002).
26. H. Zhang, W. Ding, P. Fu, X. Liu, Y. Gao, Y. Gao, Y. Cai, and Y. Yuan, "Reducing orbital angular momentum crosstalk of the Bessel-Gaussian beam for underwater optical communications," *J. Opt.* **22**, 65702 (2020).
27. Y. Yuan, T. Lei, Z. Li, Y. Li, S. Gao, Z. Xie, and X. Yuan, "Beam wander relieved orbital angular momentum communication in turbulent atmosphere using Bessel beams," *Sci. Rep.* **7**, 42276 (2017).
28. B. Miao, L. Feder, J. E. Shrock, and H. M. Milchberg, "Phase front retrieval and correction of Bessel beams," *Opt. Express* **30**, 11360 (2022).
29. K. Wulff, D. Cole, R. Clark, R. DiLeonardo, J. Leach, J. Cooper, G. Gibson, and M. Padgett, "Aberration correction in holographic optical tweezers," *Opt. Express* **14**, 4169 (2006).
30. A. Jesacher, A. Schwaighofer, S. Fürhapter, C. Maurer, S. Bernet, and M. Ritsch-Marte, "Wavefront correction of spatial light modulators using an optical vortex image," *Opt. Express* **15**, 5801 (2007).
31. Y. Liang, Y. Cai, Z. Wang, M. Lei, Z. Cao, Y. Wang, M. Li, S. Yan, P. R. Bianco, and B. Yao, "Aberration correction in holographic optical tweezers using a high-order optical vortex," *Appl. Opt.* **57**, 3618 (2018).
32. D. Armstrong, A. Stilgoe, T. Nieminen, and H. Rubinsztein-Dunlop, "Improved two-photon photopolymerisation and optical trapping with aberration-corrected structured light," *Front. Nanotechnol.* **4**, 998656 (2022).
33. N. Sanner, N. Huot, E. Audouard, C. Larat, J.-P. Huignard, and B. Loiseaux, "Programmable focal spot shaping of amplified femtosecond laser pulses," *Opt. Lett.* **30**, 1479 (2005).
34. C. Maclair, A. Mermillod-Blondin, N. Huot, E. Audouard, and R. Stoian, "Ultrafast laser writing of homogeneous longitudinal waveguides in glasses using dynamic wavefront correction," *Opt. Express* **16**, 5481 (2008).
35. C. Xie, V. Jukna, C. Milian, R. Giust, I. Ouadghiri-Idrissi, T. Itina, J. M. Dudley, A. Couairon, and F. Courvoisier, "Tubular filamentation for laser material processing," *Sci. Rep.* **5**, 8914 (2015).
36. T. Čižmár, M. Mazilu, and K. Dholakia, "In situ wavefront correction and its application to micromanipulation," *Nat. Photonics* **4**, 388 (2010).
37. H. Song, B. Liu, Y. Li, Y. Song, H. He, L. Chai, M. Hu, and C. Wang, "Practical 24-fs, 1- μ J, 1-MHz Yb-fiber laser amplification system," *Opt. Express* **25**, 7559 (2017).
38. C. Xie, R. Giust, V. Jukna, L. Furfaro, M. Jacquot, P. Lacourt, L. Froehly, J. Dudley, A. Couairon, and F. Courvoisier, "Light trajectory in Bessel-Gauss vortex beams," *J. Opt. Soc. Am. A* **32**, 1313 (2015).
39. H. Zhang, J. Xie, J. Liu, and Y. Wang, "Elimination of a zero-order beam induced by a pixelated spatial light modulator for holographic projection," *Appl. Opt.* **48**, 5834 (2009).
40. N. Xiao, C. Xie, E. Jia, J. Li, R. Giust, F. Courvoisier, and M. Hu, "Caustic interpretation of the abruptly autofocusing vortex beams," *Opt. Express* **29**, 19975 (2021).
41. A. Ovsianikov, X. Shizhou, M. Farsari, M. Vamvakaki, C. Fotakis, and B. N. Chichkov, "Shrinkage of microstructures produced by two-photon polymerization of Zr-based hybrid photosensitive materials," *Opt. Express* **17**, 2143 (2009).
42. J. Geng, X. Fang, L. Zhang, G. Yao, L. Xu, F. Liu, W. Tang, L. Shi, and M. Qiu, "Controllable generation of large-scale highly regular gratings on Si films," *Light Adv. Manuf.* **2**, 281 (2021).
43. R. Zvagelsky, F. Mayer, D. Beutel, C. Rockstuhl, G. Gomard, and M. Wegener, "Towards in-situ diagnostics of multi-photon 3D laser printing using optical coherence tomography," *Light Adv. Manuf.* **3**, 466 (2021).